MITSUBISHI ELECTRIC RESEARCH LABORATORIES
https://www.merl.com

Magnetic Flux Map Acquisition Using a Compressed Sensing Method

Patkar, Abhishek; Liu, Dehong; Wang, Yebin; Youcef-Toumi, Kamal

TR2024-107 August 07, 2024

Abstract

An accurate magnetic model for electric motors is essential for high performance control strategies. The magnetic model is typically acquired by massive experiments of measuring magnetic flux data throughout the operating current range, and then applied in the control process via a look-up table of measurements. Both the acquisition and the application processes are time-consuming and not suitable for low-latency controls. To address this issue, we propose a novel compressed sensing-based method to recover a high-fidelity flux map from limited randomly sampled data points, and further infer an analytical magnetic model of the recovered flux map. This analytical model can then be used to efficiently compute the magnetic flux instead of looking up measurement data, given the stator current in the control loop. The proposed approach is validated on data simulated by finite element analysis (FEA).

The 19th IEEE Conference on Industrial Electronics and Applications (ICIEA 2024)

Mitsubishi Electric Research Laboratories, Inc.
201 Broadway, Cambridge, Massachusetts 02139

Magnetic Flux Map Acquisition Using a Compressed Sensing Method

Abhishek Patkar
Massachusetts Institute of Technology
Cambridge, MA 02139, USA
patkar2@mit.edu

Dehong Liu
Mitsubishi Electric Research Laboratories
Cambridge, MA 02139, USA
liudh@merl.com

Yebin Wang
Mitsubishi Electric Research Laboratories
Cambridge, MA 02139, USA
yebinwang@ieee.org

Kamal Youcef Toumi
Massachusetts Institute of Technology
Cambridge, MA 02139, USA
youcef@mit.edu

***Abstract*—An accurate magnetic model for electric motors is essential for high performance control strategies. The magnetic model is typically acquired by massive experiments of measuring magnetic flux data throughout the operating current range, and then applied in the control process via a look-up table of measurements. Both the acquisition and the application processes are time-consuming and not suitable for low-latency controls. To address this issue, we propose a novel compressed sensing-based method to recover a high-fidelity flux map from limited randomly sampled data points, and further infer an analytical magnetic model of the recovered flux map. This analytical model can then be used to efficiently compute the magnetic flux instead of looking up measurement data, given the stator current in the control loop. The proposed approach is validated on data simulated by finite element analysis (FEA).**

***Index Terms*—Compressed sensing, flux maps, spatial harmonics, motor control**

I. Introduction

Electric machines are increasingly used across various areas such as factories, transportation systems, and home appliances, *etc*. A variety of electric machines such as Interior Permanent Magnet machine (IPM) and Synchronous reluctance machine (SynRM), *etc.*, have been deployed because of their high efficiency. With the advent of data driven control and an increasing demand for precise motor operation, more and more sophisticated control strategies such as Maximum Torque per Ampere (MTPA), Maximum Torque per Volts (MTPV), and Model Predictive Control (MPC) have been proposed and implemented [1], [2]. In these advanced control strategies, a common critical element to ensure high control performance is an accurate magnetic model in the control loop.

The magnetic model characterizes the magnetic flux as a function of the stator current in a reference frame of choice for 2D flux map and also as a function of the rotor angle position for 3D flux map to capture spatial harmonics. For instance, in the $d-q$ reference frame, the magnetic model for IPMs and SynRMs is highly nonlinear owing to saturation and cross-saturation effects [3]–[5]. Therefore, it is necessary to capture the non-linearity in the magnetic model to achieve good control performance. Moreover, spatial harmonics need to be considered while inferring a magnetic model as they lead to torque ripples [6], [7].

To identify the magnetic model, it is crucial to conduct experiments to acquire the magnetic flux under different currents. This is because experiments can acquire accurate and robust flux map in general. Although a viable approach to identifying the magnetic model is Finite Element Analysis (FEA) [8], FEA-based identification is typically not readily available to end users. Moreover, the FEA-based model needs to be validated through experiments to guarantee its accuracy.

However, there are two major issues for experiment-based flux map identification. First, it is very time-consuming to collect enough data for an accurate flux model. Experimental identification often requires conducting tests at sufficiently dense (I_d, I_q) grid-points to accurately capture flux variation [9]. Such a grid should span the operating range of the motor under test. For permanent magnet (PM) machines, additional care must be taken to avoid demagnetization due to overheat in experiments. To save testing time and to reduce risks of demagnetization in case of PM machines, it is thus desirable to reduce the number of tests conducted without compromising the accuracy of the acquired flux map. Second, the access speed of the flux map model is also critical for high performance control. Identified magnetic models are typically stored in a 2D or 3D look-up table. However, there is a trade-off between the access speed and the flux accuracy. To achieve an accurate flux value for a given stator current, all current-flux points in the look-up table needs to be searched to find nearby points of interest for interpolation. Both the searching process and the interpolation process are time-consuming, especially for low-latency control. Moreover, the calculation of flux map derivatives, which is required for computing control inputs, also impacts the latency of the control algorithms.

To address these issues, significant research efforts have been dedicated towards developing analytical magnetic models

This work was done when Abhishek Patkar was an intern at Mitsubishi Electric Research Laboratories.

accounting for the nonlinear effects. For instance, Ortombina *et al.* [10] proposed using Radial Basis Functions (RBFs) to get a black box model for the flux maps. Bedetti *et al.* [11] put forth a novel saturation function approach to identify the magnetic model at stand-still using just three constants. However, to capture the cross-saturation behavior, these constants that characterize self saturation behavior need to be adjusted at different test-points. Qu *et al.* [12] proposed a polynomial model to capture the nonlinear effect, treating the d, q-axis currents as a state variable and the flux as independent variables. Hinkkanen *et al.* [13] utilized the aforementioned polynomial model for self-commissioning application. All the aforementioned approaches considered saturation and cross-saturation but did not consider spatial harmonics. It is necessary to model spatial harmonics to mitigate torque ripples. Kano *et al.* [14] propose modeling the flux map using a Fourier series in the electrical angle θ and a polynomial basis in d, q-axis currents. However, to perform numerical fitting, significant data points in d, q, θ dimensions are required. Boesing *et al.* [15] also utilize Fourier series to model the θ dependence but utilize look-up tables to store Fourier coefficients to capture d, q flux variation.

This paper proposes a compressed sensing-based approach to getting an analytical expression for 2D and 3D flux maps from limited data samples. In this paper, 2D flux maps refer to the forward maps that neglect any influence of spatial harmonics, whereas 3D flux maps refer to forward maps that model the flux as a function of (I_d, I_q, θ). Compressed sensing aims to recover a sparse representation in an appropriate basis such as Fourier or wavelet basis, using limited samples of the original signal. Under certain conditions on the signal and the acquired samples, the original signal can be recovered with high probability using fewer samples than mandated by the Nyquist criterion [16], [17]. The main contributions of this paper are twofold:

1) Use much fewer randomly sampled data points than that required by Shannon-Nyquist sampling rate to build a high-fidelity 2D and 3D flux map model;
2) Provide an analytical 3D magnetic model accounting for spatial harmonics to avoid time-consuming process of searching a look-up table and interpolating nearby data points.

II. Flux map acquisition via Compressed Sensing

A. Background

A variety of signals, particularly in the audio and image domain are observed to be compressible. This implies that such signals can be accurately represented by a few active modes in an appropriate basis, such as Fourier basis, wavelet basis [18], or other learned dictionaries [19]. Compressed sensing aims to recover this sparse representation in an appropriate basis using limited samples of the original signal. In fact, in recovering sparse signals, it may be possible to relax the Shannon-Nyquist sampling theorem and the sparse signal may be recovered with high probability using fewer measurements than dictated by the Nyquist rate [20]. Compressing techniques and compressed sensing have been extensively applied for image and audio processing.

Let $x \in \mathbb{R}^n$ be a compressible signal. There exists a basis Ψ such that

$$x = \Psi s, \tag{1}$$

where $s \in \mathbb{R}^n$ is a vector whose coefficients are mostly zero or close to zero. If s has at most K non-zero elements, x is K-sparse. The measurements $y \in \mathbb{R}^p$ with $(K < p << n)$ is given by

$$y = Cx, \tag{2}$$

where $C \in \mathbb{R}^{p \times n}$ is the measurement matrix. Compressed sensing seeks to find a sparse vector $\hat{s}$ such that

$$\hat{s} = \arg\min_s ||s||_0 \quad \text{subject to } y = C\Psi s, \tag{3}$$

where $||\cdot||_0$ is the l_0 norm referring to the cardinality of s. The non-convex optimization in (3) may be relaxed to a l_1-minimization problem as

$$\hat{s} = \arg\min_s ||s||_1 \quad \text{subject to } y = C\Psi s, \tag{4}$$

where $||\cdot||_1$ is the l_1 norm given by $||s||_1 = \sum_{k=1}^{n} |s_k|$ if

1) C is incoherent with respect to Ψ
2) Number of measurements p are sufficiently large $p \approx \mathcal{O}\left(K \log\left(\frac{n}{K}\right)\right)$ [20].

In this paper, to satisfy the incoherence property, we use random samples of the flux map. We also study the variation of reconstruction error with the number of measurements.

An alternative formulation is given by

$$\hat{s} = \text{argmin}_s \frac{1}{2}||y - C\Psi s||_2 + \lambda||s||_1, \tag{5}$$

where $\lambda \geq 0$ is a regularizer weighing the importance of a sparse solution. In this paper, the formulation presented in (5) is used.

B. Compressibility of Flux Maps

In this subsection, we empirically demonstrate that q and d axis flux maps are compressible in the Fourier domain. To that end, we use readily available FEM data sets through SyR-e (Synchronous Reluctance – evolution) [21].

Let $\phi_q(I_d, I_q)$ and $\phi_d(I_d, I_q)$ denote the q and d-axis flux maps respectively. Let Φ_q and Φ_d denote the corresponding 2D Fourier spectra. For the THOR (name of a PM-SyR machine for light traction) data set chosen, we have a 31×31 data grid in (I_d, I_q) plane. Thus the Discrete Fourier Transform (DFT) of this data set will have 31×31 entries. The DFT was calculated using the Fast Fourier Transform (FFT) algorithm. Figs. 1(a) and 1(b) illustrate the Fourier coefficients arranged in decreasing order of magnitude for q, d-axis flux maps respectively. From Figs. 1(a) and 1(b), it can be seen that the magnitude of Fourier components decay rapidly in some order. Figs. 1(c) and 1(d) compare the true and compressed maps of ϕ_q. Figs. 1(e) and 1(f) compare the true and compressed maps of ϕ_d. In both cases, the compressed maps are acquired

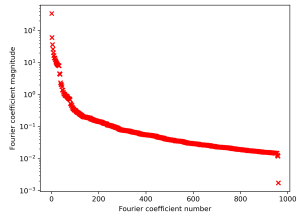

(a) q-axis Fourier coefficients arranged in descending order of magnitude

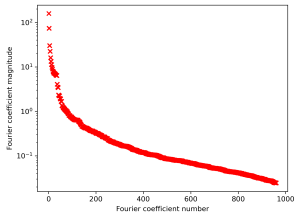

(b) d-axis Fourier coefficients arranged in descending order of magnitude

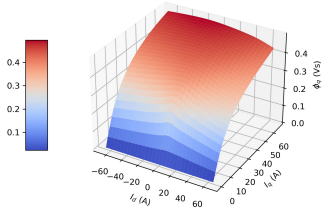

(c) True ϕ_q

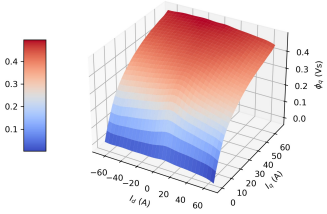

(d) ϕ_q with top 10% Fourier coefficients

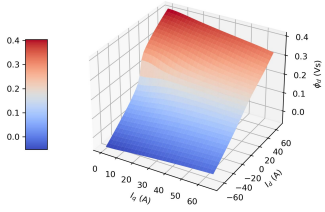

(e) True ϕ_d

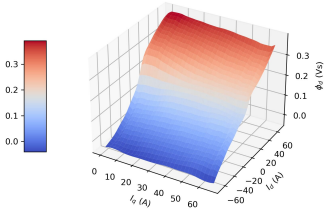

(f) ϕ_d with top 10% Fourier coefficients

Fig. 1: Compressibility of d, q-axis flux maps THOR motor

by retaining 10% of the most dominant DFT components. The Root Mean Squared Error (RMSE) in reconstructing the flux maps with dominant 10% DFT components was found to be 0.003 and 0.006 for the q and d axis respectively. From Figs. 1(c), 1(d), 1(e), and 1(f) and the low RMSE, it can be concluded that the flux maps in both d and q axes are compressible in the Fourier domain. Since all motor flux maps exhibit similar behavior, it can be empirically concluded that the 2D flux maps are compressible in Fourier domain. The number of non-zero elements of the DFT depends upon the original DFT grid and the function variation with I_d, I_q. A similar argument can be made to conclude that the 3D flux map is also compressible albeit requiring a higher number of non-zero DFT entries.

C. Mathematical Preliminaries

In this subsection, we elaborate on the relation between the flux maps and the formulation presented in (1)-(5) for the 3D case. Let ϕ be the true unknown discrete flux map with dimensions N_1, N_2, N_3 respectively. Let Φ be the corresponding Fourier transform. Partial measurements of the flux map are denoted by ϕ_p, while ϕ_{zp} denotes the map after zero-padding ϕ_p at unmeasured values. We use the subscript u to denote a matrix unrolled in column major-order into a 1-D vector. Let $\phi_u = \Psi s$ with Fourier basis Ψ and sparse vector of Fourier coefficients s. Then the flux map reconstruction problem can be formulated along (1)-(5)as

$$\hat{s} = \text{argmin}_s \frac{1}{2}||(\phi_p)_u - C\Psi s||_2 + \lambda||s||_1, \tag{6}$$

where the entries of the measurement matrix C can be readily seen as

$$C(a,b) = \begin{cases} 1 & \text{if } (\phi_p)_u[a] = \phi_u[b]. \\ 0 & \text{otherwise} \end{cases}$$

Once the sparse Fourier coefficients are achieved by solving (6), the flux map can be reconstructed as

$$\hat{\phi}_u = \Psi \hat{s}. \tag{7}$$

To help in the construction of the Fourier basis matrix Ψ, we first define the $N \times N$ DFT matrix $\boldsymbol{W}$ for an N-sample 1D signal as

$$\boldsymbol{W}_N[c,d] = W_N^{cd},$$

where $W_N = e^{-\frac{j2\pi}{N}}$. The corresponding inverse DFT matrix is given by

$$\boldsymbol{W}_N^{-1}[g,h] = \frac{1}{N}\bar{W}_N^{gh},$$

where $\bar{W}_N = e^{\frac{j2\pi}{N}}$. Now, the relationship between Φ_u and ϕ_u can then be given as

$$\Phi_u = (\boldsymbol{W}_{N_3} \otimes \boldsymbol{W}_{N_2} \otimes \boldsymbol{W}_{N_1})\phi_u, \tag{8}$$

where $\boldsymbol{W}_{N_3} \otimes \boldsymbol{W}_{N_2}$ is the kronecker product between two matrices. Now the Fourier basis matrix Ψ can be inferred as the inverse of the forward transformation in (8). Thus for the 3D case, we have

$$\Psi = \boldsymbol{W}_{N_3}^{-1} \otimes \boldsymbol{W}_{N_2}^{-1} \otimes \boldsymbol{W}_{N_1}^{-1} \tag{9}$$

The Ψ matrix for the 2D case can be computed in a similar fashion. It can be readily seen that $\Psi^{-1} = (\boldsymbol{W}_{N_3} \otimes \boldsymbol{W}_{N_2} \otimes \boldsymbol{W}_{N_1})$. While (9) defines the Fourier basis matrix for mathematical completeness, in practice, the algorithm 1 uses FFT and inverse FFT for efficient implementation.

D. Algorithm

In this subsection, the algorithm used to reconstruct the flux map from limited random samples is explained. To solve the optimization problem given in (6), a soft-thresholding based iterative algorithm is used. First, partial measurements of the flux map ϕ_p are zero-padded at unknown values to get the zero-padded flux map ϕ_{zp}. The reconstructed flux map $\hat{\phi}$ is then initialized as ϕ_{zp}. Next, the flux map is transformed into the sparse Fourier domain using FFT. Soft-thresholding is then applied in the Fourier domain. After applying inverse FFT, data consistency is enforced to make sure the entries that are measured are consistent across ϕ_p and $\hat{\phi}$. The iterative algorithm runs until convergence, which is determined by ϵ, a parameter chosen a priori.

Algorithm 1 Flux map reconstruction using CS

Input: $\phi_p, \lambda, \epsilon$

Procedure:

$\phi_{zp} \leftarrow \phi_p$ ▷ Zero pad measured flux map

$\hat{\phi}_0 \leftarrow \phi_{zp}$ ▷ Initialize reconstructed map

while $\frac{||\hat{\phi}_i - \hat{\phi}_{i-1}||}{||\hat{\phi}_i||} \geq \epsilon$ **do**

$(\hat{\Phi}_{i-1})_u = \Psi^{-1}(\hat{\phi}_{i-1})_u$ ▷ To Fourier domain

$(\Phi_i)_u \leftarrow S((\hat{\Phi}_{i-1})_u, \lambda)$

$(\hat{\phi}_i)_u \leftarrow \Psi(\Phi_i)_u$

if $(\phi_{zp})_u[j] == 0$ **then**

$(\hat{\phi}_i)_u[j] \leftarrow (\hat{\phi}_{i-1})_u[j]$

else

$(\hat{\phi}_i)_u[j] \leftarrow (\phi_{zp})_u[j]$ ▷ Enforce data consistency

end if

end while

Output: $\hat{\phi}$

$S(u, \lambda)$ is a soft-thresholding function defined as

$$S(u,\lambda) = \begin{cases} 0 & \text{if } |u| \leq \lambda \\ \frac{|u|-\lambda}{|u|} u & \text{if } |u| > \lambda. \end{cases} \tag{10}$$

Here $|\cdot|$ computes the absolute value and the threshold λ is the regularizing parameter used in (6). The threshold λ is empirically tuned. To begin with, the threshold may be set to 5% of the maximum DFT coefficient of ϕ_{zp}.

III. Results and Discussion

The proposed compressed sensing-based approach described in section II is applied to reconstruct 2D and 3D flux maps using FEM data.

A. 2D Flux Map reconstruction

The THOR and syreDefaultmotor datasets, available in Syre in the PM orientation, are used as simulation data. The flux map data for the THOR motor is available as a function of $\{I_d, I_q, \theta\}$ in a $31\times31\times180$ grid respectively. The 2D flux map is calculated by averaging along θ axis, given $\phi_q(I_d, I_q)$ and $\phi_d(I_d, I_q)$ respectively. Thus this flux map consists of 961 data points on a grid for I_d from -66.11A to 66.11A and I_q from 0A to 66.11A. First, 40% of data points are randomly sampled from the available flux map to get $\phi_{qp}(I_q, I_d), \phi_{dp}(I_q, I_d)$. In experimental flux map identification, this operation would correspond to acquiring flux data at random I_d, I_q grid-points. The algorithm proposed in section II is then applied to reconstruct the flux map at the missing grid points.

Figs. 2(a) and 2(c) depict the random samples across the I_d, I_q grid used to reconstruct the q and d-axis flux maps, respectively. Figs. 2(b) and 2(d) show the corresponding reconstructed flux maps. Comparing Fig. 1(c) with Fig. 2(b) and Fig. 1(e) with Fig. 2(d), it can be concluded that the 2D flux maps for the THOR motor can be recovered reasonably well from 40% random samples. Figs. 2(e) and 2(f) showcase the low reconstruction error between the true and reconstructed flux map in the q and d axis respectively. For representation purposes, a similar ϕ axis scale is used between Figs. 2(a), 2(e) and Figs. 2(d), 2(f) respectively.

Fig. 3 showcases the variation of the root mean squared error (RMSE) between the true and reconstructed flux maps as function of the percentage of data points used for reconstruction. It is evident that the reconstruction RMSE decreases with an increase in the percentage of data points used for reconstruction. However, the marginal improvement in RMSE diminishes with an increase in the percentage of data points used for reconstruction. This trend is expected as an increase in the number of known data points implies less missing information and hence better identification. Since the flux maps are sparse in Fourier domain, once the dominant Fourier components have been identified, a further increase in the number of data points provided would lead to identification of less significant Fourier components implying diminishing improvement in reconstruction error.

Finally, to demonstrate the generalizability of our method, we repeat the analysis to reconstruct the q-axis flux map on a different motor dataset. We use the syreDefaultMotor dataset for this p. Fig. 4(a) showcase the random samples used to reconstruct the q-axis flux map for the syreDefaultMotor. Based on Figs. 4(b), 4(c), and 4(d), it is evident that the proposed method generalizes well in reconstructing the flux maps.

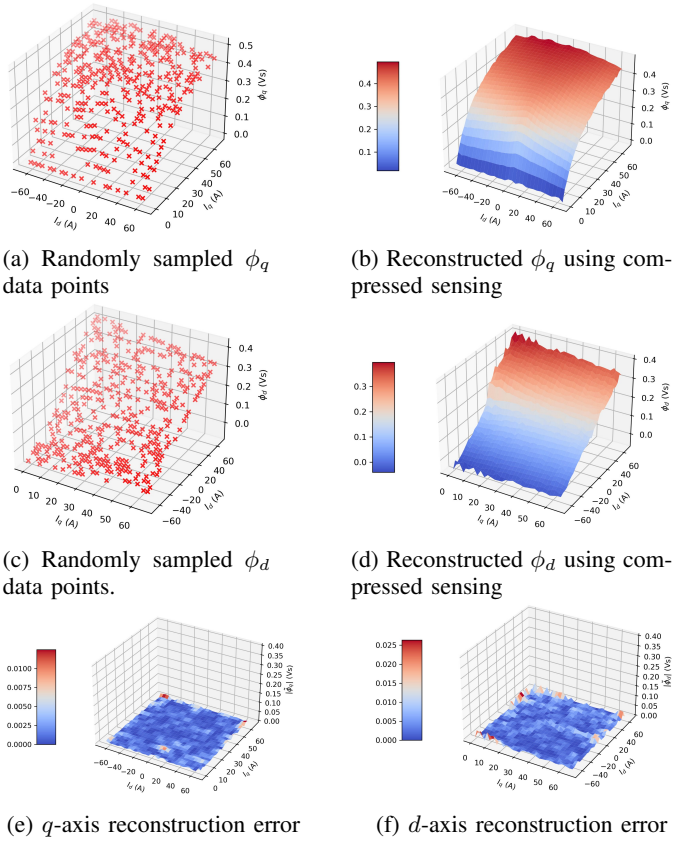

(a) Randomly sampled ϕ_q data points

(b) Reconstructed ϕ_q using compressed sensing

(c) Randomly sampled ϕ_d data points.

(d) Reconstructed ϕ_d using compressed sensing

(e) q-axis reconstruction error

(f) d-axis reconstruction error

Fig. 2: q, d-axis flux map reconstruction using compressed sensing on THOR dataset

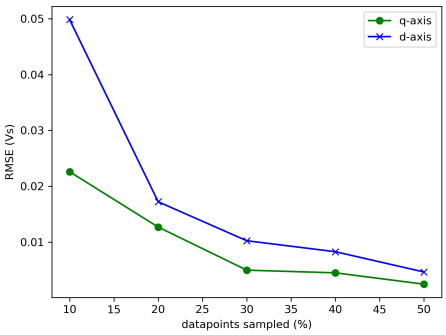

Fig. 3: Reconstruction RMSE for ϕ_q, ϕ_d as a function of $\%$ data points provided

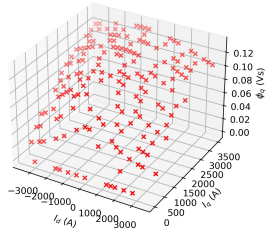

(a) SyreDefault motor randomly sampled ϕ_q data points

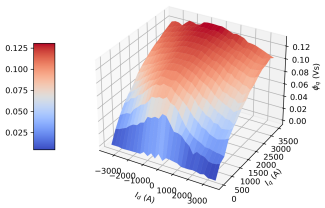

(b) SyreDefault motor reconstructed ϕ_q using compressed sensing

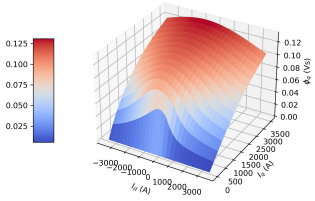

(c) SyreDefault motor true ϕ_q

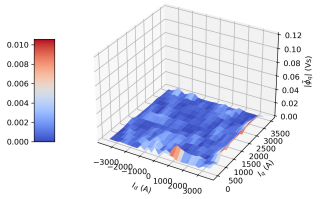

(d) SyreDefault motor ϕ_q reconstruction error

Fig. 4: q-axis flux map reconstruction using compressed sensing on SyreDefault dataset

Thus in practice, the number of (I_d, I_q) grid points at which tests need to be conducted to acquire flux map is reduced significantly.

B. 3D Flux Map reconstruction

Having demonstrated the effectiveness of the proposed approach in reconstructing 2D flux maps, we apply it to reconstruct 3D flux maps and to acquire an analytical expression for 3D flux maps. The THOR data-set is once again used as simulation data. At every (I_d, I_q) grid point, we use just 9 random samples over $[0, 2\pi]$. The algorithm proposed in 1 is then applied to reconstruct the 3D flux map. Fig. 5(a) illustrates the true flux variation, the random samples used and the reconstructed flux map variation in the q axis with respect to θ at a fixed (I_d, I_q) grid point. To highlight the reconstruction using limited sampling, we also include linear

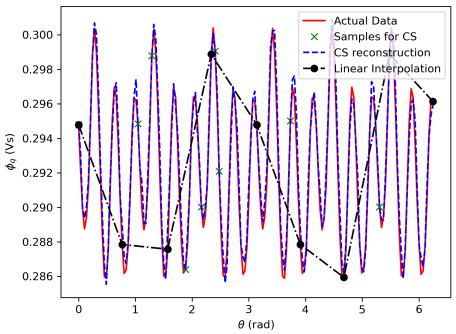

(a) Variation of ϕ_q with θ at $I_d = 39.7\text{A}$, $I_q = 17.6\text{A}$

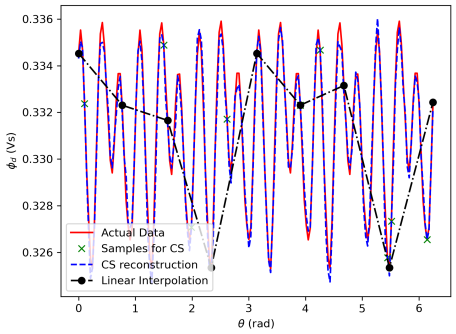

(b) Variation of ϕ_d with θ at $I_d = 39.7\text{A}, I_q = 17.6\text{A}$

Fig. 5: q, d-axis flux variation with θ at a particular (I_d, I_q) grid-point

interpolation of 9 equi-spaced samples. Similarly, Fig. 5(b) illustrates the aforementioned quantities for the d axis.

The RMSE between the true and CS reconstructed flux map is found to be 0.0011 and 0.0009 for q, d axis respectively. The RMSE between the true and linear interpolation flux map is found to be 0.0053 and 0.0043 for q, d axis respectively. Thus we can see that the CS reconstruction reduces the error by approximately 5 times in both q, d axis. From Figs. 5(a),5(b) and the low reconstruction RMSE, it can be concluded that the spatial harmonic behavior at different values of (I_d, I_q) can be modelled using few 3D Fourier coefficients. The compressed sensing based approach can be applied to reconstruct the 3D flux map using few random samples along θ at each grid-point (I_d, I_q). It is also evident from Figs. 5(a) and 5(b) that linear interpolation with the same number of equi-spaced random samples does not capture the harmonic variation.

To acquire an analytical expression for the 3D flux map, we leverage the fact that the maps are sparse in the Fourier domain and simplify using the Fourier basis to represent the signal. For ease of representation and to enable further simplification, we utilize the unrolled representation of the inverse Fourier transform instead of the one given in (9). We demonstrate the procedure on the q-axis flux map; a similar procedure can be adopted to acquire the analytical expression for the d-axis flux map. Let $\mathbf{Z}$ be the matrix of Fourier coefficients for the q-

axis flux map. The analytical expression can be simply written using the inverse Discrete Fourier transform expression as

$$\phi_q(n_1,n_2,n_3) = \sum_{a=0}^{N_1-1}\sum_{b=0}^{N_2-1}\sum_{c=0}^{N_3-1}\frac{Z(a,b,c)}{N_1N_2N_3}\cdot e^{\{2\pi j[\frac{an_1}{N_1}+\frac{bn_2}{N_2}+\frac{cn_3}{N_3}]\}}, \quad (11)$$

where N_1, N_2, and N_3 correspond to the size of $\{I_d\}$,$\{I_q\}$, and $\{\theta\}$, respectively, and n_1,n_2, and n_3 correspond to the indices for the flux map under consideration, respectively. Note that n_1, n_2, n_3 are all integer numbers, corresponding to discrete current and angle. In case of motor control, the d,q-axis currents and the angle are real numbers. In this situation, we simply replace the integer indices (n_1, n_2, n_3) by real numbers $(\tilde{n}_1, \tilde{n}_2, \tilde{n}_3)$ corresponding to the real measurements. For real parameters (I_d, I_q, θ) with $I_d \in [-I_{dmax}, I_{dmax}], I_q \in [0, I_{qmax}], \theta \in [0, \theta_{max}]$, $\tilde{n}_1, \tilde{n}_2, \tilde{n}_3$ can be calculated as

$$\begin{cases} \tilde{n}_1 &= \frac{(I_d+I_{dmax})(N_1-1)}{2I_{dmax}}, \\ \tilde{n}_2 &= \frac{I_q(N_2-1)}{I_{qmax}}, \\ \tilde{n}_3 &= \frac{\theta(N_3-1)}{\theta_{max}}. \end{cases} \quad (12)$$

Note that $\mathbf{Z}$ is a sparse matrix, meaning that most entries of $\mathbf{Z}$ are zero. Leveraging this sparsity of $\mathbf{Z}$ and combining (11) and (12), we can write the analytical magnetic flux model as

$$\tilde{\phi}_q(I_d,I_q,\theta) = \sum_{Z(a,b,c)\neq 0}\frac{Z(a,b,c)}{N_1N_2N_3}\cdot e^{\{2\pi j[\frac{a(I_d+I_{dmax})}{2I_{dmax}}\frac{N_1-1}{N_1}+\frac{bI_q}{I_{qmax}}\frac{N_2-1}{N_2}+\frac{c\theta}{\theta_{max}}\frac{N_3-1}{N_3}]\}}. \quad (13)$$

Thus (13) provides a compact analytical function of flux maps accounting for spatial harmonics, which can be utilized to compute flux value efficiently in the control loop without using a lookup table.

IV. Conclusion

In this paper, a novel compressed sensing based approach was proposed to reconstruct 2D and 3D flux maps using a small number of measurements of the map. Results using FEM simulation data show that the entire 2D flux map could be reconstructed with high accuracy using just 40% of data points. Thus such an approach would reduce the number of grid points that need to be tested while conducting experimental flux map identification. Furthermore, analytical expressions of flux maps are achieved by leveraging the sparsity of flux maps in Fourier basis. Such analytical expressions would be particularly useful in model-based control strategies such as MTPA and MPC, etc.

References

[1] Q. Liu and K. Hameyer, "High-performance adaptive torque control for an IPMSM with real-time MTPA operation," *IEEE Transactions on Energy Conversion*, vol. 32, no. 2, pp. 571–581, 2017.

[2] C. Jia, X. Wang, Y. Liang, and K. Zhou, "Robust current controller for IPMSM drives based on explicit model predictive control with online disturbance observer," *IEEE Access*, vol. 7, pp. 45 898–45 910, 2019.

[3] P. Guglielmi, M. Pastorelli, and A. Vagati, "Cross-saturation effects in IPM motors and related impact on sensorless control," *IEEE Transactions on Industry Applications*, vol. 42, no. 6, pp. 1516–1522, 2006.

[4] B. Stumberger, G. Stumberger, D. Dolinar, A. Hamler, and M. Trlep, "Evaluation of saturation and cross-magnetization effects in interior permanent-magnet synchronous motor," *IEEE Transactions on Industry Applications*, vol. 39, no. 5, pp. 1264–1271, 2003.

[5] N. Bianchi and S. Bolognani, "Magnetic models of saturated interior permanent magnet motors based on finite element analysis," in *Conference Record of 1998 IEEE Industry Applications Conference. Thirty-Third IAS Annual Meeting (Cat. No.98CH36242)*, vol. 1, 1998, pp. 27–34 vol.1.

[6] J. Lee, Y.-C. Kwon, and S.-K. Sul, "Identification of IPMSM flux-linkage map for high-accuracy simulation of IPMSM drives," *IEEE Transactions on Power Electronics*, vol. 36, no. 12, pp. 14 257–14 266, 2021.

[7] X. Chen, J. Wang, B. Sen, P. Lazari, and T. Sun, "A high-fidelity and computationally efficient model for interior permanent-magnet machines considering the magnetic saturation, spatial harmonics, and iron loss effect," *IEEE Transactions on Industrial Electronics*, vol. 62, no. 7, pp. 4044–4055, 2015.

[8] G. Bramerdorfer, S. M. Winkler, M. Kommenda, G. Weidenholzer, S. Silber, G. Kronberger, M. Affenzeller, and W. Amrhein, "Using FE calculations and data-based system identification techniques to model the nonlinear behavior of PMSMs," *IEEE Transactions on Industrial Electronics*, vol. 61, no. 11, pp. 6454–6462, 2014.

[9] E. Armando, R. I. Bojoi, P. Guglielmi, G. Pellegrino, and M. Pastorelli, "Experimental identification of the magnetic model of synchronous machines," *IEEE Transactions on Industry Applications*, vol. 49, no. 5, pp. 2116–2125, 2013.

[10] L. Ortombina, F. Tinazzi, and M. Zigliotto, "Magnetic modeling of synchronous reluctance and internal permanent magnet motors using radial basis function networks," *IEEE Transactions on Industrial Electronics*, vol. 65, no. 2, pp. 1140–1148, 2018.

[11] N. Bedetti, S. Calligaro, and R. Petrella, "Stand-still self-identification of flux characteristics for synchronous reluctance machines using novel saturation approximating function and multiple linear regression," *IEEE Transactions on Industry Applications*, vol. 52, no. 4, pp. 3083–3092, 2016.

[12] Z. Qu, T. Tuovinen, and M. Hinkkanen, "Inclusion of magnetic saturation in dynamic models of synchronous reluctance motors," in *2012 XXth International Conference on Electrical Machines*, 2012, pp. 994–1000.

[13] M. Hinkkanen, P. Pescetto, E. Mölsä, S. E. Saarakkala, G. Pellegrino, and R. Bojoi, "Sensorless self-commissioning of synchronous reluctance motors at standstill without rotor locking," *IEEE Transactions on Industry Applications*, vol. 53, no. 3, pp. 2120–2129, 2017.

[14] Y. Kano, K. Watanabe, T. Kosaka, and N. Matsui, "A novel approach for circuit-field-coupled time-stepping electromagnetic analysis of saturated interior PM motors," *IEEE Transactions on Industry Applications*, vol. 45, no. 4, pp. 1325–1333, 2009.

[15] M. Boesing, M. Niessen, T. Lange, and R. De Doncker, "Modeling spatial harmonics and switching frequencies in PM synchronous machines and their electromagnetic forces," in *2012 XXth International Conference on Electrical Machines*, 2012, pp. 3001–3007.

[16] D. Donoho, "Compressed sensing," *IEEE Transactions on Information Theory*, vol. 52, no. 4, pp. 1289–1306, 2006.

[17] E. Candes, J. Romberg, and T. Tao, "Robust uncertainty principles: exact signal reconstruction from highly incomplete frequency information," *IEEE Transactions on Information Theory*, vol. 52, no. 2, pp. 489–509, 2006.

[18] E. Candes and J. Romberg, "Sparsity and incoherence in compressive sampling," *Inverse problems*, vol. 23, no. 3, p. 969, 2007.

[19] I. Tošić and P. Frossard, "Dictionary learning," *IEEE Signal Processing Magazine*, vol. 28, no. 2, pp. 27–38, 2011.

[20] S. L. Brunton and J. N. Kutz, *Data-Driven Science and Engineering: Machine Learning, Dynamical Systems, and Control*. Cambridge University Press, 2019.

[21] G. P. Simone Ferrari. Synchronous reluctance evolution (syr-e). [Online]. Available: https://github.com/SyR-e/syre_public